Automatic Segmentation of Overlapping Cervical Smear Cells based on Local Distinctive Features and Guided Shape Deformation

Afaf Tareef[a,*], Yang Song[a], Weidong Cai[a], Heng Huang[b], Hang Chang[c], Yue Wang[d], Michael Fulham[e], Dagan Feng[a], Mei Chen[f,g]

[a] *Biomedical and Multimedia Information Technology (BMIT) Research Group, School of Information Technologies, University of Sydney, Australia.*
[b] *Department of Computer Science and Engineering, University of Texas, USA.*
[c] *Life Sciences Division, Lawrence Berkeley National Laboratory, USA.*
[d] *Bradley Department of Electrical and Computer Engineering, Virginia Polytechnic Institute and State University, USA.*
[e] *Department of PET and Nuclear Medicine, Royal Prince Alfred Hospital, Australia, and Sydney Medical School, University of Sydney, Australia.*
[f] *Department of Informatics, University of Albany State University of New York.*
[g] *Robotics Institute, Carnegie Mellon University, USA.*

Abstract

Automated segmentation of cells from cervical smears poses great challenge to biomedical image analysis because of the noisy and complex background, poor cytoplasmic contrast and the presence of fuzzy and overlapping cells. In this paper, we propose an automated segmentation method for the nucleus and cytoplasm in a cluster of cervical cells based on distinctive local features and guided sparse shape deformation. Our proposed approach is performed in two stages: segmentation of nuclei and cellular clusters, and segmentation of overlapping cytoplasm. In the first stage, a set of local discriminative shape and appearance cues of image superpixels is incorporated and classified by the Support Vector Machine (SVM) to segment the image into nuclei, cellular clusters, and background. In the second stage, a robust shape deformation framework is proposed, based on Sparse Coding (SC) theory and guided by representative shape features, to construct the cytoplasmic shape of each overlapping cell. Then, the obtained shape is refined by the Distance Regularized Level Set Evolution

*Corresponding author
Email address: atar8654@uni.sydney.edu.au (Afaf Tareef)

(DRLSE) model. We evaluated our approach using the ISBI 2014 challenge dataset, which has 135 synthetic cell images for a total of 810 cells. Our results show that our approach outperformed existing approaches in segmenting overlapping cells and obtaining accurate nuclear boundaries.

Keywords: overlapping cervical smear cells, feature extraction, sparse coding, shape deformation, distance regularized level set.

---

1. Introduction

Cervical cancer is a malignant tumor of the cervix and is the fourth most common cause of cancer death in women worldwide [1]. Cervical cancer, however, can be effectively treated if it is detected early during a routine Pap smear test. In the test, a sample of cells from the cervix is smeared, or spread, onto a glass slide, and examined under a microscope for nuclear and cytoplasmic atypia to detect pre-cancerous abnormalities in cervical cells based on the shape variations of the nuclei and cytoplasm. The automated segmentation of overlapping cells remains one of the most critical challenges in the analysis of microscopic cervical images [2].

Although there has been substantial progress in the segmentation of cervical cells, unfortunately, the state-of-the-art approaches tend to underperform on images with overlapping cells. There are currently four main categories of techniques to segment cervical cells and they include the segmentation of: a) isolated or free-lying cells without any overlapping between the cells [3, 4, 5, 6, 7, 8, 9, 10]; b) isolated and overlapping nuclei [11, 12, 13, 14, 15, 16, 17, 14]; c) overlapping nuclei and the whole cellular clusters consisting a number of cells [18, 19]; and d) nuclei and cytoplasm from a cluster of overlapping cells [4, 20, 21, 22, 2].

In this paper, we propose a two-stage segmentation technique for the nuclei and cytoplasm of overlapping cells. We have incorporated discriminative shape and appearance cues that sufficiently distinguish the nuclei and the background in superpixel representation level. These superpixel-based features are then used to train the supervised SVM to separate the nuclei and cell clusters

from the background. In the second stage, there is a cytoplasmic segmentation using sparse shape deformation that is guided toward the target shape using representative features captured from a well-established initial shape. The obtained shape is refined by the distance regularized level set evolution (DRLSE) model to obtain more accurate cell segmentation.

2. Literature review

The classic approach for segmenting the isolated cervical cells is the thresholding method [3]. This method, however, leads to unsatisfactory results due to the complex structure of cervix cells resulted from the poor contrast and variable staining. Marker-based and multi-scale watersheds have also been used to segment the cytoplasm [4]. Watershed segmentation treats the image intensity as a topographic relief that is filled by water from different minima, and then assigns the same label to all regions associated with the same catchment basin. The main limitation of watershed-based segmentation techniques is the over-segmentation of cells. Active contour model (ACM), or 'snakes', is another family of segmentation techniques widely used to segment cervical cells [5, 6, 7]. In ACMs, a curve or a surface is evolved under a constraint toward the object boundary. ACMs are able to recover closed object boundaries with pixel accuracy. These approaches, however, are insufficient for touching and overlapping cell segmentation.

A number of methods to segment isolated and overlapping nuclei have been proposed based on thresholding and morphological analysis [11], active contours [12], level set [13], adaptive active shape model [14], watershed transform [15, 16], and unsupervised classification [17]. For instance, Plissiti et al. [14] used an adaptive active shape model trained on a set of images each with a single nucleus, and the attributes of the nuclear shapes are expressed to estimate the shape model distribution, which is used to detect the unknown overlapping nuclei boundaries.

There are also approaches to segment the overlapping nuclei and cellular

clusters from the background. Gentav et al. used an unsupervised approach with automatic thresholding to separate cells from background, a multi-scale hierarchical watershed segmentation algorithm and a binary classifier to separate nuclei from cellular cytoplasm [18]. Kale and Aksoy applied a multi-scale watershed algorithm to initially segment the image, and then SVM to finish the segmentation [19]. Despite the good performance of these approaches in segmenting nuclei and single cells, they are not able to delineate the boundary of each individual overlapping cytoplasm, which is a critical deficiency as the shape of the cytoplasm is an important feature for subsequent cellular analysis.

Segmentation of both nuclei and cytoplasm from overlapping cells in Pap smears is a great challenge due to the large variation in shape and obscure boundary. Recently, a limited number of techniques have been suggested to segment overlapping cervical cells [4, 20, 21, 22, 2]. An early technique [4] used a locally constrained watershed transform to segment partially overlapping cells. However, it cannot be used for cells with a large overlapping area. Another automated segmentation approach proposed by Tareef et al. [20] was based on gradient thresholding and morphological operations. This approach worked for the overlapping cells with noticeable difference in intensities; however, it was not effective with large fuzzy clusters of small cells.

Recently, shape constrained deformation model has been successfully used for medical image segmentation, where shape priors are learned from a set of training samples and used on optimization methods, such as Active Shape Model (ASM) [23], sparse shape model [45, 28, 25], and level set evolution with shape priors [24, 26, 27]. Some recent methods have tended to segment the overlapping cervical cells by incorporating an ellipsoidal shape prior [21] and a star shape prior [22] with level set optimization for more accurate cell segmentation. Lu et al. [21] proposed an overlapping cell segmentation technique incorporating ellipsoidal shape prior with a joint level set optimization, constrained by the intensity of the overlapping region, the length and area of each cell, and the amount of cell overlap. A new improved version of this approach is presented in [2] where a joint optimization of multiple level set functions is utilized with

unary (intracell) constraints computed based on contour length, edge strength, and cell shape, and pairwise (intercell) constraints computed based on the area of the overlapping regions. Although this approach achieved good results for the overlapping cells, there is a high degree of false negatives owing to the failure in segmenting some complicated cells.

The situation for cervical smears also applies to other cytological examinations. Investigators have suggested a segmentation technique for overlapping cells of breast tissue microarrays and blood smears [29]. The centers of regions containing densely touching and overlapping cells were detected using single pass voting with mean-shift-based seed detection. Then a level set algorithm based on an interactive model generated the contour of each cell using the obtained centers as an initial position. Srisang et al. suggested a technique for chromosomes based on Voronoi diagrams and Delaunay triangulations [30]; with this technique, overlapping chromosomes are cut into two chromosomes by identifying all possible cut points from the contour line of overlapping chromosomes to select four target cut points to separate the overlapping chromosomes. Quelhas et al. proposed a sliding band filter (SBF) based approach [31] to detect convex shapes corresponding to the nucleus by analyzing the local convergence of image gradients to estimate the cytoplasm shape. In [26, 27], a boundary and region-based active contour model incorporating shape priors in a level set evolution was used to segment overlapping nuclei in histopathology images of breast and prostate biopsy specimens. However, these techniques may not work effectively with Pap smears as cervical cells have a greater degree of overlap than the examples in which these other techniques have been used.

3. The proposed overlapping nucleus and cytoplasm segmentation approach

Accurate cervical cell segmentation should be able to identify background cells and the nucleus and cytoplasm of individual cells. The proposed workflow of our method is shown in Figure 1 with nuclear and cellular cluster segmentation

in the first stage and then segmentation of the overlapping cytoplasm in the second stage. A pre-processing step is also carried out. The algorithm is outlined in Table 1.

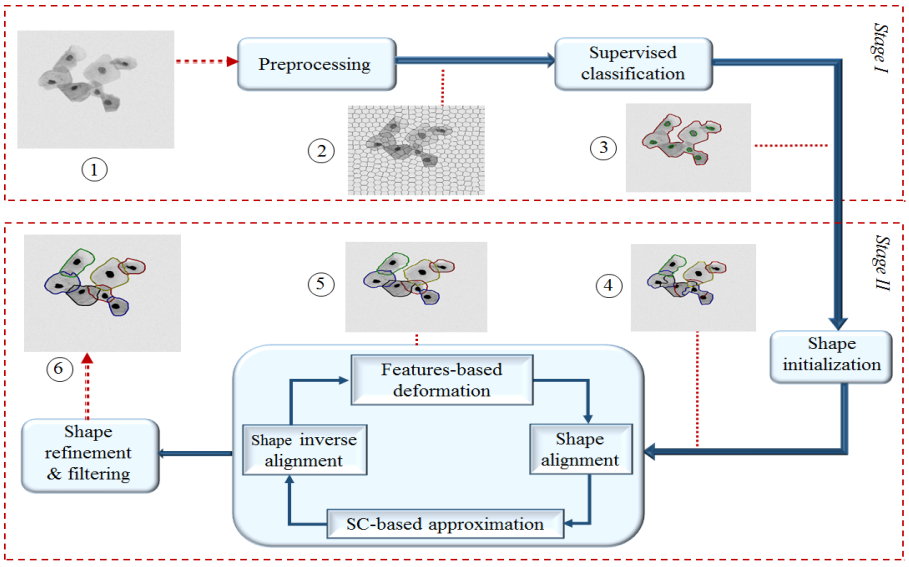

Figure 1: Our approach is shown across the six sub-components in two stages: (1) original Pap smear image, (2) pre-processed image, (3) nuclei (green) and cellular clusters (red) segmentation results using the local superpixel-based features to train SVM, (4) initial shape: the detected closed regions surrounding nuclei that are used in sparse shape approximation, (5) constructed cytoplasm shape using SC with a training shape dictionary guided by robust feature points F_p of the initial shape and, (6) final segmentation after the DRLSE-based refinement and candidate filtering.

3.1. Pre-processing

To achieve better classification, we chose to work at the superpixel level instead of at the pixel-grid level for the underlying representation. Superpixels represent the homogenous regions by integrating the local intensity and position information, and hence, the features extracted at the superpixel-level can better describe the difference between the local regions. Superpixels preserve image boundaries since the boundaries of the superpixels closely match true image

Table 1: The proposed approach for overlapping cells segmentation

Pseudo-code
Input: Pap smear image
Output: Individual nucleus and cytoplasm of free-laying and overlapping cells.
Stage I: Nuclei and cellular clumps segmentation
1. Compute SLIC superpixel map from I
2. pre-process to eliminate the noise and highlight the edges
3. Extract shape, texture, and boundary features, and train SVM. Assume N is the number of nuclei detected in this stage
Stage II: Cytoplasm segmentation
for i = 1 to N
If isolated cell: go to step (9), **else**:
1. Generate two edges maps, and complete the missed edges if needed
2. Generate the initial cytoplasmic shape based on the closed contour objects included in a computed ROI
3. Extract the feature points F_p of the initial cytoplasmic shape that most likely represent the target contour
4. Sparse approximate the starting sparse shape using the feature points F_p and the sub-dictionary Φ_F to get the sparse solution X_F. Then, the initial shape is reconstructed using the most relative shapes in Φ by $Y_o = \Phi X_F$
for j =1 to predefined number of SC iterations
5. Sparse deform the cell shape using the shape templates in the dictionary Φ
6. Deform the output shape Y_o based on the feature points. F_p coordinates are used to construct the transformation aligning the output shape to the target shape space
7. Assign F_p to the corresponding points of the output shape to reserve the shape information
8. Apply the moving average filter on the output shape to recognise the shape connectivity and regularity requirement
end
9. Refine the deformed shape by DRLSE
10. Filter out the small candidates based on a present threshold
end

boundaries, and they also reduce the computational cost. The difference in the superpixel shapes also helps distinguish local regions and this is the principle of the designed shape descriptor we use in our approach.

For the pre-processing step, we use the simple linear iterative clustering (SLIC) algorithm [32] to segment the image into local smooth regions corresponding to nuclei, cellular clusters, and background. SLIC algorithm guarantees more regular shapes for smooth regions when appropriate superpixel size and regularizer value were used. Fragmenting the Pap image into regularly-shaped superpixels makes it easier to differentiate the nuclei and background based on the superpixel shape. In some cases, the nucleus may be divided into two superpixels affecting the elliptical shape property. However, most of the nuclei superpixels can still be correctly classified based on the superpixel-level texture and boundary features. For instance, the nucleus (a) in Figure 2 was divided into two superpixels, where both have a lower intensity, smoother texture, and more boundary pixels than the surrounding cytoplasm superpixels. Thus, the two superpixels representing the nucleus (a) are correctly classified as nuclei superpixels as shown in Figure 1 (3). The output of this step is a map of superpixels, with each superpixel labelled with an integer number in the range [1, $\#SP$], where $\#SP$ is the total number of superpixels in the image determined by SLIC algorithm.

To enhance the appearance of the image and reduce the noise, an image I is convolved with a Gaussian filter and equalized by the Contrast-Limited Adaptive Histogram Equalization (CLAHE) [33] with a small threshold γ, i.e., 0.005 to enhance the nuclei that have poor contrast due to cytoplasmic overlap. The reason for generating superpixels prior to this enhancement step is to prevent over-segmenting the cytoplasm and including dark regions around the nuclei in the nuclear superpixels (see Fig 2).

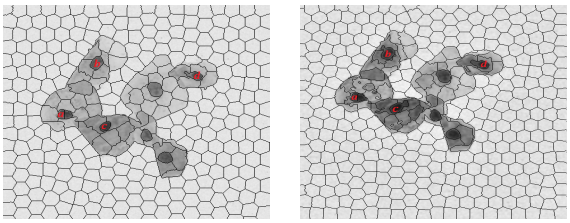

(a) (b)

Figure 2: The SLIC superpixel maps of the Pap image in Fig 1-(1): (a) before and (b) after pre-processing step. Superpixeling after pre-processing leads to over-segment some dark regions (which become darker with image equalization), or include them in the nuclear superpixels, e.g., nucleus a, b, c, and d.

3.2. Nuclei and Cellular Cluster Segmentation based on Distinctive Superpixel-level Cues with SVM

The aim here was to separate the nuclei and cell clusters from the background. For each superpixel S_i, local superpixel shape, texture, and boundary cues are extracted, and arranged into feature vector. The criteria of our feature design are based on textural and geometrical differences between the superpixels, e.g. the nuclei superpixels tend to have an elliptical shape, whereas cytoplasmic superpixels usually have irregular shapes. In these instances, the eccentricity and minor axis length of the superpixels provide a good descriptor. Figure 3 shows the feature extraction process. The shape, texture, and boundary features obtained from the superpixel S_i are combined into the feature vector $f(S_i)$:

$$f(S_i) = [f_{shap}(S_i)\ f_{text}(S_i)\ f_{bound}(S_i)] \tag{1}$$

3.2.1. Shape features

Referring to Figure 3, the shapes of SLIC superpixels are heterogeneous, as the nuclear superpixels tend to be elliptical, whereas the shape of the background superpixels is hexagonal and the cytoplasm is irregular. Thus, two sufficient shape features are derived: the minor axis length (L_m), and excessive lengthening or eccentricity (EC). The minor axis length L_m is the length (in

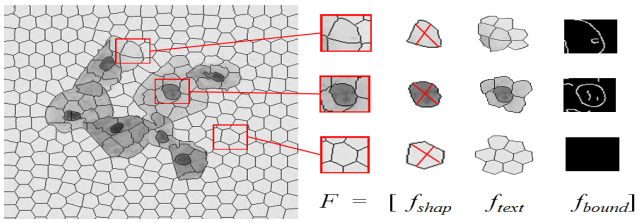

Figure 3: Feature extraction procedure: (a) the superpixel map of image containing seven overlapping cells, (b) local representitive shape, texture, and boundary features are extracted from each superpixel.

pixels) of the shortest diameter of an ellipse completely enclosing the superpixel region, whereas eccentricity $EC = \sqrt{1-(L_m/L_x)^2} \in [0,1]$ is the ratio of the distance between the foci of the superpixel and its major axis length L_x, which provides a good information about the circularity of the superpixel [34]. The shape features are arranged in vector f_{Shap} as following:

$$f_{Shap}(S_i) = [L_m(S_i) \;\; EC(S_i)] \tag{2}$$

3.2.2. Texture features

Nuclear superpixels are generally distinguished by a homogenous texture and a low intensity value compared to neighbouring superpixels. Therefore, a set of histogram-based features along with a comparative feature are used to capture texture properties of the superpixels. Four standard texture features were extracted: the mean value $(\bar{.})$ and standard deviation σ of the pixel intensities, the median of gradient magnitude $M(\nabla)$, where ∇ donates the gradient operator, and the entropy H of the superpixel S_i are used for the superpixel texture [35]. We also used a comparative feature $\delta(S_i, B_i) = |M(B_i) - M(S_i)|$ that measures the change in the intensity between the superpixel S_i and its boundary interface B_i pixels located within a pre-defined Euclidean distance, i.e., 5, from S_i. The texture feature vector can thus be written as:

$$f_{text}(S_i) = [\bar{S}_i \;\; \sigma(S_i) \;\; M(\nabla S_i) \;\; H(S_i) \;\; \delta(S_i, B_i)] \tag{3}$$

3.2.3. Boundary features

The boundary features are designed to distinguish the nuclear and the cellular cluster superpixels, which are the most important superpixels for the next stage. Generally, most edges in the image are found around the nuclei and the cellular clusters. Even if the background has some edges generated by noise, they would be short and unconnected edges. The pre-processing step also helps in reducing the background noise and highlights the nuclei and cluster boundaries. To this end, we chose two boundary features: the number of edges in the superpixel, and the length of each edge, where each connected and isolated edge is considered as a single edge. The edge map was obtained using Canny edge detector [36] with 0.1 threshold, and then, the connected components in the edge map are labelled and counted as described in [37]. The boundary features help in distinguishing the superpixels belonging to nuclei and those belonging to the cellular clusters and background. The number of connected edges (E_N) in the superpixel, and the length of them (E_{len}) (i.e., number of pixels in each edge) are computed and combined as a boundary feature vector formed as:

$$f_{bound}(S_i) = [E_N(S_i)\, E_{len}(S_i)] \tag{4}$$

3.2.4. Classification

Finally, the extracted superpixel-based feature vectors are used to classify the image superpixels as background, cytoplasm, and nuclei superpixels. For classification, we chose a linear Support Vector Machine (SVM) classifier, specifically, C-support vector classification (C-SVC) algorithm provided by LIBSVM software package [38] with a regularization parameter C equals 1. The SVM classifier was trained on all labelled SLIC superpixels of the training images. SVM has been widely used in image segmentation and it has proven effectiveness in handling the complex segmentation problems in microscopy images [39, 40, 41, 42].

3.3. Overlapping Cell Segmentation based on Guided Shape Approximation and DRLSE Model

In this stage, cell contours of the detected nuclei are delineated by shape initialization, approximation, and deformation processes. The cytoplasm shape of each overlapping cell can be estimated by establishing a closed region surrounding each detected nucleus representing the initial cytoplasm, and sparse shape learning based on training shapes along with representative features. Finally, the obtained shape is refined by DRLSE for more accurate segmentation. The overlapping cell segmentation stage is divided into an edge-based shape initialization, a guided Sparse Coding (SC) based shape deformation, and DRLSE-based refinement with candidate filtering.

3.3.1. Edge-based shape initialization

In this step the initial shape of the cytoplasm is established based on the closed contour objects. First, isolated cells are identified based on the number of nuclei in a cluster classified in the previous stage. For isolated cells, the initial contours of the DRLSE model are directly formed by the morphological holes filling of the cluster's boundary edges. In this case, there is no need for a sparse coding based cytoplasm deformation as the cell boundary is identified in the classification stage.

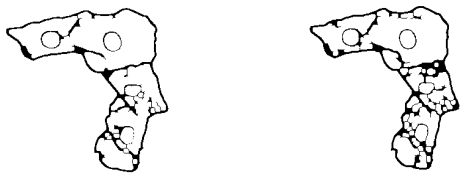

(a) (b)

Figure 4: Example of edges map generated with (a) upper threshold, and (b) lower threshold. In this case, the first edges map has many missing pixels affecting the segmentation output, whereas the other edges map can provide a good initialization for the overlapping cells.

If the cellular cluster has two or more nuclei, then, the Canny edge detector is applied to extract the cell edges. Given the complexity of cervical images, it is difficult to identify the boundaries of all cells in one image using a single threshold. For instance, the boundaries of touching or overlapping cells with noticeable differences in intensities can be identified using the Canny detector with a high threshold. Whereas, a fuzzy cellular cluster, with convergent intensities and unclear edges, requires a low threshold to obtain more detailed edges to generate a connected region. On the other hand, excessive edge detail will not give a correct description for the touching or less-overlapping cells since the edges may divide a cell into multiple parts or lead to inclusion of a part of the attached cell into the cell in focus. Since prior determination of the class of each cell in the image is difficult, we chose to establish two cell edge maps using two different thresholds: an upper threshold β_u and a lower threshold β_l, where only one edge map will be used to generate the initial cell mask. The results of this step are two skeletonized edge maps for each cell, generated by applying Canny detector twice with upper and lower thresholds on the complement of the cellular cluster (i.e., to reduce the appearance of noise), and linked by closing the edges (with a disk with radius C_r) after removing the short ones. Finally, the nuclei boundaries and unlinked edges are removed to get connected edge maps as shown in Figure 4.

Based on careful analysis of the geometric structure of cervical cells, we propose to determine the cytoplasmic region of each nucleus dynamically based on the surrounding edges, positioned in a reasonable Euclidean distance Γ, excluding the nuclear boundary. For each nucleus n in the overlapping cluster, a circular region-of-interest (ROI) with radius r from its centroid is determined. Usually, the mean radius is used in the literature to determine the ROI [43], which gives a reasonable initialization of the cell with a semi-circular shape and nucleus positioned in the center of the cell. However, the cervical cells have a multiform shape, and hence, using the mean radius to determine the ROI may lead to exclude part of the cell from the searching area. Based on our empirical analysis, the ROI radius r in our approach is computed as the average of the

longest radial length (r_x) and the mean of the most frequent radial lengths (r_M) included in Γ, with higher weight to r_x to cope with cell shape variations (see Figure 5(a)):

$$r\left(n\right) = \left(2 \times r_x\left(n\right) + r_M\left(n\right)\right)/3 \tag{5}$$

The cell masks, indicating the cell area associated with n, are simply generated by the morphological holes filling and closing of the edge maps within the computed ROI, and picking the rough mask with the largest convex area after eliminating the candidates whose area and circularity are smaller than thresholds (i.e., $\tau_c = 0.15$ and $\tau_a = 0.01$ of the whole image size, respectively). If the first edge map (i.e., generated by the upper threshold β_u) passes this step, the generated cell mask is used as an initial cell shape for the subsequent steps, otherwise, both edge maps are fused together by pixel-wise Exclusive-OR operator, and used to produce the cell mask. In cases where the fused edge map also fails to generate the initial mask due to the absence of a large number of boundary pixels or the high irregularity, a contour with ROI radius r is connected to the contour pixels of the first edge map (e.g., the green line in Figure 5(b)).

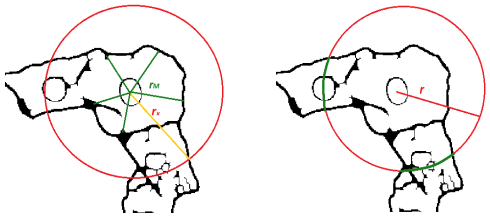

(a) (b)

Figure 5: (a) Determining the radius of the cell region, the green lines represent the most frequent distances, and the yellow line represents the maximum distance, (b) the circular ROI where the cytoplasm masks will be found, the green line shows how the boundary is closed in case of missing edges.

3.3.2. Guided SC-based shape deformation

Figure 6 shows the SC-based shape approximation flowchart, where the input shape can be deformed under guidance of the initial shape features and a dictionary constructed from the annotated training cell shapes. To illustrate, assume S denotes a 2D input shape represented by the coordinates of N contour points extracted, aligned, and arranged in a vector $Y = [x_1, y_1, x_2, y_2, ..., x_N, y_N]^T \in \mathbb{R}^{2N}$, containing the x-y coordinates of contour points. Let $\Phi = [\Phi_1, \Phi_2, ..., \Phi_M] \in \mathbb{R}^{2N \times M}$ is the shape dictionary consisting of M pre-aligned and arranged training shape instances from annotated training dataset (i.e., 270 shape instances for our experiments). Then, the shape S can be approximately represented as a linear combination of relatively few atoms in the training shape dictionary. Mathematically, the approximation of S by Φ can be formulated as the following sparse coding problem:

$$\arg\min_{X} \|Y_T - \Phi X\|_2^2 \qquad s.t. \qquad \|X\|_0 < s \tag{6}$$

where Y_T is an aligned version of the input shape using Procrustes' analysis [44] with the reference training shape to transform shapes into a standard coordinate system. $X \in \mathbb{R}^{M \times 1}$ is the sparse representation of Y_T with s non-zero entries, i.e., s=5. Sparse coding has been successfully used in many segmentation problems [45, 46, 47, 48]. However, these approaches have been designed for objects with shapes of relatively small variation from their typical templates (e.g., the lung and heart). The large shape variation and the high degree of overlap of cervical smear cells make it difficult to apply the existing SC-based approaches to our segmentation problem.

Training stage

Consider we have M training cervical cells $\{C_1, C_2, ..., C_M\}$ and their labelled ground truth, the shape vector for each training cell is generated by concatenating the 2D coordinates of N edge points closing the cell shape, i.e., $N = 360$ edge points, obtained by extracting one point at each degree along the

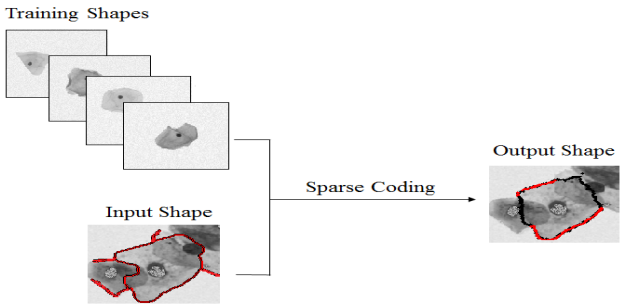

(a) (b)

Figure 6: SC-based shape approximation: (a) the shape dictionary and the input shape generated by the edge-based shape initialization process, (b) the output shape where the red points represent the feature points F_p used to supervise the sparse shape approximation process.

cell contour, originated from the nucleus center. One of these training shapes is chosen as the reference shape used to perform Procrustes' analysis to transform each training shape to the space of the reference shape. Let the aligned shapes be denoted as $\{C_i^A, i = 1, ..., M\}$. To remove the bias from the selection of reference, the mean of the aligned training shape is chosen as the new reference $S_r = \sum_{i=1}^{M}(C_i^A)/M$, and the alignment process is performed again using the new reference. Finally, the aligned shapes are arranged in vector (i.e., $S_i = [x_{i1}, y_{i1}, x_{i2}, y_{i2}, ..., x_{iN}, y_{iN}], i = 1, ..., M$), and stored in the shape dictionary.

Deformation stage

Firstly, a set of feature points of the initial shape used to guide the approximation process is determined. In detail, the contour points of the initial shape, which belong to the boundary between the cellular cluster and background that are included in a narrow cytoplasmic domain $\Gamma - \varepsilon$ (i.e., to avoid the outliers), are marked as characteristic feature points F_p, e.g. the red points in Figure 7(b). Given that the contour points of the regular cell mask generated by the first edge map is most likely representing the true cytoplasmic contour, they

can be also used as feature points of the generated initial shape. The extracted feature points are used to guide the next shape deformation procedures.

The cytoplasm deformation starts by constructing the starting sparse shape using only F_p of the initial shape. The sparse solution of F_p is computed using a sub-dictionary containing only the corresponding points to F_p for all training instances in the shape dictionary (Φ_F), which can be simply extracted using the feature points indices. The sparse solution $X_F \in \mathbb{R}^{M\times 1}$ is computed as following:

$$\arg\min_{X_F} \|F_{pT} - \Phi_F X_F\|_2^2 \qquad s.t. \qquad \|X_F\|_0 < s \tag{7}$$

where F_{pT} is the aligned version of F_p by Procrustes' analysis using the corresponding points in the reference shape S_r using the feature points indices. Stagewise Orthogonal Matching Pursuit (StOMP) [49] is used in our approach to find X_F due to its low computational complexity and attractive asymptotic statistical properties. Next, using the full shape prior dictionary (Φ), the shape contour can be approximated using few non-zero coefficients of the sparse solution:

$$Y_o = \Phi X_F \tag{8}$$

To force the approximation process toward the desired shape, two subsequent procedures are iteratively performed: contour points-based sparse approximation, followed by F_p-based deformation process. In the contour points-based approximation process, the earlier procedures shown by Eq. (7) and Eq. (8) are repeated using all cell contour points (i.e., 360 points). Then, F_p-based deformation process is performed to restrict the sparse shape for the actual cell shape, which can be partially represented by the feature points.

Particularly, the coordinate positions of F_p and the corresponding points of the output shape Y_o are used to compute the similarity mapping transformation T_s that minimizes the least squares error between them [50]. The obtained transform T_s is then applied to the output shape points transferring them to the correct space of the feature points to result in the transformed shape Y_{oT}.

Let this be denoted by $T_s Y_o$, where T_s consists of $(h_x, h_y, \sigma, \theta)$ transformations; h_x and h_y represent the translation in x and y axis, σ represents the scale, and θ represents the rotation angle.

In practice, the transformed shape Y_{oT} tends to take an elliptical shape changing the coordinates of some feature points. To keep the distinctive shape information and adjust the shape variation in cervical cells, the feature points F_p are assigned to the corresponding points in Y_{oT}, and then, the new output shape coordinates are smoothed by the moving average filter [51] to recognise the shape connectivity and regularity. This approximation process (i.e., contour points-based sparse approximation followed by F_p-based deformation) is repeated K times to obtain more accurate segmentation.

Figure 1 shows that our guided SC-based shape approximation provides a good segmentation and the approximated contour of each cell is very close to the target contour. However, we expect some pixels of the background or neighboring cells to be included within the estimated contour. Thus, DRLSE is used to address this issue and provide a more reliable segmentation for the actual boundary of the cell in focus.

3.3.3. DRLSE-based refinement and candidate filtering

This step aims to refine the segmented cell mask to remove excess pixels connected to the cell boundary, mainly, background pixels included in cytoplasm superpixels in the first stage and misclassified as cytoplasm pixel, and then, filter out the cytoplasm candidate that is smaller than being a cell. To highlight some light cytoplasmic pixels close to the background pixels, only the cellular clusters of the image are equalized by CLAHE. Finally, the obtained cell contour is refined by a geodesic active contour model, and then, the false cytoplasm candidates, whose areas are smaller than a size threshold, are removed. The Distance Regularized Level Set Evolution (DRLSE) model [52] is chosen for cell refinement, where a distance regularization term is defined with a potential function, such that the derived level set evolution has a unique forward-and-

backward (FAB) diffusion effect, maintaining a desired shape of the level set function (LSF). DRLSE forces the curve to evolve near the signed distance function, and thus, guarantees curve smoothness and eliminates the need for the costly reinitialization procedure. Consider that $\phi : \Omega \rightarrow \mathbb{R}$ denotes a LSF on a domain Ω. The energy functional to be minimized is defined as:

$$\varepsilon = \mu\mathcal{R}(\phi) + \lambda(L)(\phi) + \alpha\mathcal{A}(\phi) \tag{9}$$

where μ, λ, and α are constants (i.e., $\mu = 0.2, \lambda = 5, \alpha = 1.5$). $\mathcal{R}(\phi)$ is a regularization term maintaining the signed distance property $\nabla\phi = 1$ to guarantee the smoothness, $\mathcal{L}(\phi)$ measures the length of the zero level, and $\mathcal{A}(\phi)$ measures the area of $\phi < 0$. The energy functional $\varepsilon(\phi)$ can be minimized by solving the following gradient flow:

$$\frac{\partial\phi}{\partial t} = \mu div\left(d_p(|\nabla\phi|\nabla\phi) + \lambda\delta_\epsilon(\phi)div\left(g\frac{\nabla\phi}{|\nabla\phi|}\right) + \alpha g\delta_\epsilon(\phi)\right. \tag{10}$$

where $\delta(.)$ is the Dirac delta function, and g is the edge stopping function defined as:

$$g\left(|\nabla I|\right) = \frac{1}{1 + |\nabla G_\sigma \times I|^2} \tag{11}$$

where G_σ is the Gaussian kernel with standard deviation σ, and I is the image on a domain Ω.

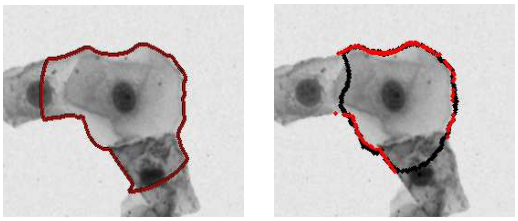

(a) (b)

Figure 7: (a) The initial shape using for shape approximation, (b) the approximated cytoplasm shape using sparse coding. Red points represent the feature points F_p which are used to guide the sparse approximation process.

4. Material and evaluation methods

We evaluated the performance of our approach using the dataset and evaluation methodology of the ISBI 2014 "Overlapping Cervical Cytology Image Segmentation Challenge" [53], with 135 synthetic gray-scale images (i.e., 45 training images and 90 test images) artificially produced from real, free-lying cervical cells. The total number of the nuclei and cytoplasm pairs in the images is 810 (i.e., 270 training cells and 540 test cells), and the image size is 512×512 pixels. We used the training dataset to train the SVM classifier and generate the shape dictionary, whereas the test dataset is used for performance evaluation.

Object-level and pixel-level measures were used to assess the segmentation results. We used criteria developed by Gentav et al. [18] to evaluate the quantitative performance of the nuclear segmentation. Considering the segmented nucleus region O_d and the corresponding ground-truth O_{gt}, a good nuclear segmentation is the one satisfying the following condition:

$$\frac{O_d \cap O_{gt}}{O_d} > 0.6 \quad and \quad \frac{O_d \cap O_{gt}}{O_{gt}} > 0.6 \tag{12}$$

Based on Eq. (12), the segmented nuclei are classified as object-level true positive (TP_O), false negative (FN_O) or false positive (FP_O); they are used to compute the object-level precision ($P_{Obj.}$) and recall ($R_{Obj.}$) values using the following equations:

$$P_{Obj.} = TP_O/(TP_O + FP_O) \tag{13}$$

$$R_{Obj.} = TP_O/(TP_O + FN_O) \tag{14}$$

The pixel-level precision ($P_{Pix.}$) and recall ($R_{Pix.}$) values are calculated for the good segmentations that were determined using the Dice Coefficient (DC). DC was computed as:

$$DC = 2\ \frac{\#\{O_d \cap O_{gt}\}}{\#\{O_d\} + \#\{O_{gt}\}} \tag{15}$$

A 'good' segmentation is considered to be the one with a DC value greater than 0.7. For cytoplasm segmentation, the object-level performance was evaluated using the false negative rate; pixel-level performance was assessed using the true positive rate, false positive rate and DC, using the evaluation code provided by the challenge.

5. Experimental results and discussion

To evaluate the proposed methodology, we measured the object-level and pixel-level segmentation performance for the nuclei and cytoplasm, the performance over different cell structures, and the computational cost of the proposed approach. We also discussed the performance improvement of our guided deformation process over the conventional deformation process. Further, we compared our cytoplasm segmentation results to the results of the ISBI challenge winners applied on the same ISBI test and train datasets: a) Ushizima's segmentation approach [54], based on nuclear narrow-band seeding, graph-based region growing and Voronoi diagrams; and b) Nostrati's approach [55], based on maximally stable extremal region detector (MSER), random decision forest classifier (RF), and signed distance map (SDM) function. We also compared our nuclei and cytoplasm segmentation results to the results of the baseline approach proposed by the ISBI challenge organizers [2].

The main parameters of our method, which may significantly influence the segmentation performance, are summarized in Table 2. The parameters used by our approach were chosen based on our initial validation study on a sample of the training and test images. For instance, the superpixel size was selected based on the size of the nuclei in the dataset, if a smaller superpixel size was used, some nuclei regions would be divided into two or more superpixels, and thus, the elliptical shape of the nuclei would be lost. Also a lower regularizer value could lead to over-segmentation of nuclei regions. A higher equalization threshold in the pre-processing step could increase the intensity of some regions and result in classifying them as nuclei by the SVM. Moreover, it is important

that the radius of the initial region corresponds to the cell size in the dataset, so that two or more overlapping cells are not treated as the one cell. The value of the initial radius is based on the size of the cells in the dataset, thus, it should be properly tuned to suit other datasets, likewise, the minimum cell size which is based on our test cells. We also used secondary parameters including $\beta_u = 0.1$, $\beta_l = 0.01$, $C_r = 3$, and $\varepsilon = 10$ used in edge establishment. The proposed approach is less sensitive to reasonable changes in these parameters, and hence, these parameters may work with other datasets. For instance, our approach has the potential to provide a good cell segmentation as long as the canny thresholds used in edge establishment are able to provide enough feature points to represent the cell shape, noting that most of these feature points are extracted from the cellular cluster boundary obtained from SVM classification stage. Parameter sensitivity analysis is provided in Table 5.

Table 2: Parameters

Our approach steps	Parameters	Value
Stage I	Superpixel size	25
	Regularizer value	0.01
Stage II	Initial radius Γ	90
	SC iterations K	5
	DRLSE iterations	50 (Narrowband)
	Minimum cell size	0.01 of image size

5.1. Evaluation of Nuclei Segmentation

The nuclear segmentation results are shown in Table 3. A segmented nucleus was considered as a true positive if the overlapping ratio computed by Eq. (12) is larger than 0.6, causing under-segmented nuclei to be counted as false negatives. Nevertheless, our results had a good true positive rate indicated by the recall value of 0.94, with on average 6% improvement over the recall obtained by Lu et al. at 0.88. Our method also had a high precision of 0.99, compared to Lu et al.'s method with a low false positive rate. Our technique missed only

31 true nuclei out of 540 nuclei in all images. Our false negative results are mainly related to the similarity of texture and density between the nuclei and the surrounding cytoplasm. There were only 8 false positive nuclei; four were true nuclei but they did not satisfy Eq. (12) as they missed some true pixels or included some boundary surface pixels.

Given the importance of identifying nuclei in discriminating normal from abnormal cells in a Pap smear, a reliable approach should also have high pixel-level segmentation performance. Table 3 shows that our approach had a high pixel-based precision of 0.95 ($\pm$0.06), recall of 0.93 ($\pm$0.07) and DC values of 0.93 ($\pm$0.05), whereas the precision, recall, and DC values obtained by Lu et al.'s approach were 0.94 ($\pm$0.08), 0.91 ($\pm$0.08) and 0.92 ($\pm$0.05), respectively.

Table 3: Object-level and pixel-level Nuclei segmentation results

The approaches	$P_{Obj.}$	$R_{Obj.}$	$P_{Pix.}$	$R_{Pix.}$	DC
Lu's approach [2]	0.98	0.88	0.94 $\pm$ 0.08	0.91 $\pm$ 0.08	0.92 $\pm$ 0.05
Our approach	**0.99**	**0.94**	0.95 $\pm$ 0.06	**0.93 $\pm$ 0.07**	**0.93 $\pm$ 0.04**

Incorporating shape and appearance features in superpixel level were the main contributing factor to our better performance in the object-level and pixel-level nuclei segmentation. Figure 8 illustrates the performance of our incorporated features in classifying the superpixels. We compared the object-level nuclei segmentation precision and recall using texture and boundary features (T_B), texture and shape features (T_Sh), and all the features (All). The combination of shape and appearance features All improved recall from 0.91 to 0.94, and there was a small improvement in precision. Nucleus superpixels were distinguished from the other superpixels by low intensity, homogenous texture, clear boundaries and an elliptical shape, which all were represented by our features.

5.2. Evaluation of Cytoplasm Segmentation

The cytoplasm segmentation results of our approach compared to the challenge are shown in Table 4. Our method had the highest pixel-level true positive rate of 0.91 ($\pm$0.09) with up to an 8% improvement over the challenge results.

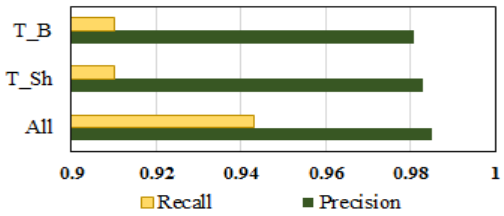

Figure 8: Object-level nuclei segmentation results using different features.

The DC of 0.89 ($\pm$0.07) surpassed Ushizima and Nostrati et al.'s techniques by about 2%. Our object-based false negative FNo rate was also lower than Lu et al.'s techniques.

In general, increasing the pixel-based true positive rate TPp also increased the false positive rate FPp, and vice versa. Ushizima et al.'s technique had the lowest FPp rate but at the expense of having the lowest TPp rate of 0.83. Our method had the highest TPp without increasing the false positive limit. Likewise, TPp and DC were negatively related to FNo. The high TPp and DC of Lu et al.'s approach were associated with the high FNo. We had a similar DC to Lu et al., but with higher TPp and lower FNo. Our method was twice as fast as Lu et al., and we had better nuclear segmentation results as shown in the previous section. Our guided shape deformation improved the cytoplasm segmentation because it excluded the false regions close to the cell boundary, where conventional deformable models stop or move slowly. We present further discussion on the performance of our guided shape deformation in Section 5.3 and 5.5. Furthermore, Table 5 shows the cytoplasm segmentation performance of our approach using different secondary parameters. The results in the table proved the reliability of our proposed approach, where the pixel-based measures are in the same high range with different parameters. It is worth mentioning that the qualitative segmentation results for the cases in Table 5 are changed (i.e., the best qualitative results were obtained by the parameters used in our approach), however, the overall quantitative results are still in the same range.

Table 4: Cytoplasm segmentation results

The approaches	DC	TPp	FPp	FNo
Ushizima's approach [54]	0.87 ± 0.08	0.83± 0.13	**0.002 ± 0.002**	0.17± 0.21
Nostrati's approach [55]	0.87 ± 0.07	0.90 ± 0.08	0.005 ± 0.004	**0.14 ± 0.16**
Lu's approach [2]	0.89 ± 0.08	0.90 ± 0.10	0.003 ± 0.005	0.31 ± 0.29
Our approach	**0.89 ± 0.07**	**0.91 ± 0.09**	0.004 ± 0.005	0.27 ± 0.28

Table 5: Parameter sensitivity analysis.

β_u	β_l	C_r	ε	DC	TPp	FPp	FNo
0.05	0.005	2	10	0.88 ± 0.08	0.91 ± 0.09	0.004 ± 0.005	0.26 ± 0.26
0.05	0.01	3	15	0.88 ± 0.07	0.92 ± 0.08	0.005 ± 0.005	0.23 ± 0.25
0.05	0.05	2	10	0.88 ± 0.08	0.91 ± 0.09	0.004 ± 0.005	0.27 ± 0.27
0.01	0.001	3	5	0.89 ± 0.07	0.91 ± 0.09	0.004 ± 0.005	0.27 ± 0.28
0.01	0.001	5	15	0.88 ± 0.08	0.90 ± 0.09	0.005 ± 0.005	0.25 ± 0.26
0.01	0.05	3	5	0.89 ± 0.07	0.91 ± 0.09	0.004 ± 0.005	0.28 ± 0.30
0.05	0.01	3	15	0.88 ± 0.07	0.90 ± 0.09	0.004 ± 0.005	0.29 ± 0.28
0.01	0.001	3	10	0.89 ± 0.07	0.91 ± 0.09	0.004 ± 0.005	0.27 ± 0.28

5.3. Evaluation of Segmentation for Different Cell Structures

The ISBI dataset was grouped according to the complexity of the cells structure, represented by the number of cells in each image and the overlapping ratios between the cells, into 45 groups. The number of cells in each Pap image is varied between 2 and 10 cells, where each cell overlap with at least one cell in the same image with an overlap ratio in one of the following ranges: [0, 0.1, 0.2, 0.3, 0.4]. We also chose to further evaluate our segmentation performance on images of different groups. The results are summarized in Table 6. The results demonstrated that our approach is not much sensitive to changes in the number of cells in the images, whereas, a consistent improvement in performance was shown when the overlapping ratio was decreased. According to the results, our approach successfully segmented cell clusters with a large number of cells (between 8 and 10 cells) provided the overlapping ratios between the cells is in the range $[0, 0.2]$. Our method worthily segmented the cytoplasm of isolated and touching cells (i.e., zero overlap ratio) with a very high DC rates of 0.93-0.96,

regardless the number of cells in a single image. The pixel-based false positive rate FPp for this group was low, i.e., 0.001, with high TPp rate of 0.93, on average. The FNo was also small at 0.01. Furthermore, the segmentation of the cells with overlapping ratio $\in \{0.1, 0.2\}$ was also effective with TPp of 0.90 and DC of 0.87, on average. The good results in these cases were mainly due to the clarity of the cell boundaries, resulting in enough feature points to guide our deformation process toward the real cell shape.

The most problematic case occurred when we have a large fuzzy cell clusters with unclear edges, thus, insufficient number of feature points can be extracted. There was a high FNo of 0.44, on average, for this case (i.e., overlapping ratio $\in \{0.3, 0.4\}$). Nevertheless, our approach still got a good DC of 0.86, and acceptable FPp of 0.006. Moreover, the obtained TPp was 0.89, which was still higher than the TPp value obtained by [54] ISBI approach.

Figure 9 shows examples of our segmentation results for a different number of cells and degree of cell overlap. The first group of images in the figure shows our segmentation results for Pap images with overlapping ratio $\in \{0, 0.1, 0.2\}$. The second group shows the segmentation results for the difficult cases, where the overlapping ratio $\in \{0.3, 0.4\}$. It can be seen that our approach can provide an accurate, and sometime semi-optimal, segmentation for the free-lying and slightly overlapping cells. In addition, our segmentation for the overlapping cluster of multiple cells is still good. The second group of images includes some of our failure cases, which mainly occurred when the feature points of the cell were not enough to represent the cell shape, especially, when if the cell was irregularly-shaped. Also, when the cell nucleus is located in one side of the cell, this may lead to inaccurate determination of ROI radius, resulting in excluding part of the cell from the searching area, e.g., the cell highlighted by black line in Figure 9 (g). Such this case probably can be controlled by taking an error percentage into consideration when the standard deviation of the radii in the cell exceed a threshold.

For more evaluation, a qualitative comparison of the nuclei and cytoplasm segmentation of our approach and the ISBI approaches is provided in Figure 10

using the visual results provided by the ISBI organizers [56]. As seen in the figure, the proposed approach provided the best, and semi-optimal, segmentation for the overlapping cells in the first image. Moreover, the proposed approach gives better segmentation for the overlapping areas in the second image than the ISBI approaches. However, parts of two cells in the second image (i.e., highlighted by green and red lines in our results) were mis-segmented due to excluding them from the ROI in edge establishment step. This case mainly occurred when the cell nucleus is located in one side of the cell, thus, the mean radius used in Eq. (5) mislead the ROI radius computation.

Table 6: The cytoplasm segmentation results for different cell structure.

	Overlapping ratio				
	0	0.1	0.2	0.3	0.4
2 cells	DC=.94, TP_p=.92, FP_p=.001, FN_o=.00	DC=.94, TP_p=.93, FP_p=.001, FN_o=.00	DC=.95, TP_p=.92, FP_p=.001, FN_o=.00	DC=.92, TP_p=.90, FP_p=.002, FN_o=.25	DC=.84, TP_p=.86, FP_p=.006, FN_o=.00
3 cells	DC=.95, TP_p=.93, FP_p=.001, FN_o=.00	DC=.87, TP_p=.92, FP_p=.004, FN_o=.00	DC=.86, TP_p=.95, FP_p=.008, FN_o=.17	DC=.88, TP_p=.91, FP_p=.004, FN_o=.17	DC=.82, TP_p=.95, FP_p=.012, FN_o=.17
4 cells	DC=.96, TP_p=.93, FP_p=.000, FN_o=.00	DC=.94, TP_p=.94, FP_p=.002, FN_o=.12	DC=.88, TP_p=.86, FP_p=.002, FN_o=.50	DC=.86, TP_p=.89, FP_p=.005, FN_o=.13	DC=.85, TP_p=.94, FP_p=.007, FN_o=.37
5 cells	DC=.96, TP_p=.93, FP_p=.000, FN_o=.00	DC=.88, TP_p=.90, FP_p=.004, FN_o=.10	DC=.83, TP_p=.87, FP_p=.006, FN_o=.10	DC=.87, TP_p=.85, FP_p=.003, FN_o=.20	DC=.84, TP_p=.77, FP_p=.001, FN_o=.80
6 cells	DC=.94, TP_p=.94, FP_p=.001, FN_o=.00	DC=.91, TP_p=.93, FP_p=.004, FN_o=.00	DC=.88, TP_p=.88, FP_p=.004, FN_o=.33	DC=.90, TP_p=.91, FP_p=.004, FN_o=.58	DC=.84, TP_p=.85, FP_p=.005, FN_o=.58
7 cells	DC=.93, TP_p=.91, FP_p=.001, FN_o=.00	DC=.93, TP_p=.95, FP_p=.002, FN_o=.00	DC=.88, TP_p=.92, FP_p=.005, FN_o=.29	DC=.83, TP_p=.89, FP_p=.007, FN_o=.71	DC=.85, TP_p=.91, FP_p=.008, FN_o=.36
8 cells	DC=.96, TP_p=.95, FP_p=.001, FN_o=.00	DC=.84, TP_p=.92, FP_p=.006, FN_o=.00	DC=.84, TP_p=.87, FP_p=.006, FN_o=.31	DC=.82, TP_p=.84, FP_p=.007, FN_o=.44	DC=.85, TP_p=.95, FP_p=.013, FN_o=.56
9 cells	DC=.95, TP_p=.95, FP_p=.001, FN_o=.00	DC=.84, TP_p=.90, FP_p=.007, FN_o=.28	DC=.89, TP_p=.89, FP_p=.003, FN_o=.28	DC=.85, TP_p=.89, FP_p=.006, FN_o=.33	DC=.91, TP_p=.90, FP_p=.003, FN_o=.78
10 cells	DC=.95, TP_p=.93, FP_p=.001, FN_o=.05	DC=.87, TP_p=.88, FP_p=.004, FN_o=.10	DC=.83, TP_p=.84, FP_p=.005, FN_o=.20	DC=.86, TP_p=.91, FP_p=.007, FN_o=.70	DC=.86, TP_p=.85, FP_p=.004, FN_o=.65
Average	DC=.95, TP_p=.93, FP_p=.001, FN_o=.01	DC=.88, TP_p=.91, FP_p=.004, FN_o=.07	DC=.86, TP_p=.88, FP_p=.005, FN_o=.24	DC=.86, TP_p=.88, FP_p=.005, FN_o=.39	DC=.85, TP_p=.90, FP_p=.007, FN_o=.48

5.4. Evaluation of the Computational Cost

The execution time (second per cell) of each major step in our approach is shown in Table 7. The time was obtained using non-optimized MATLAB code on a PC with a 3.2GHz Intel Core i5 processor and 8GB RAM. The edge establishment time in the table includes the execution time of the isolated cells segmentation, edge detection and linking, ROI determination, establishing the initial shape, and the alternative shape initialization process. The sparse deformation time is the execution time of the test phase in the SC-based defor-

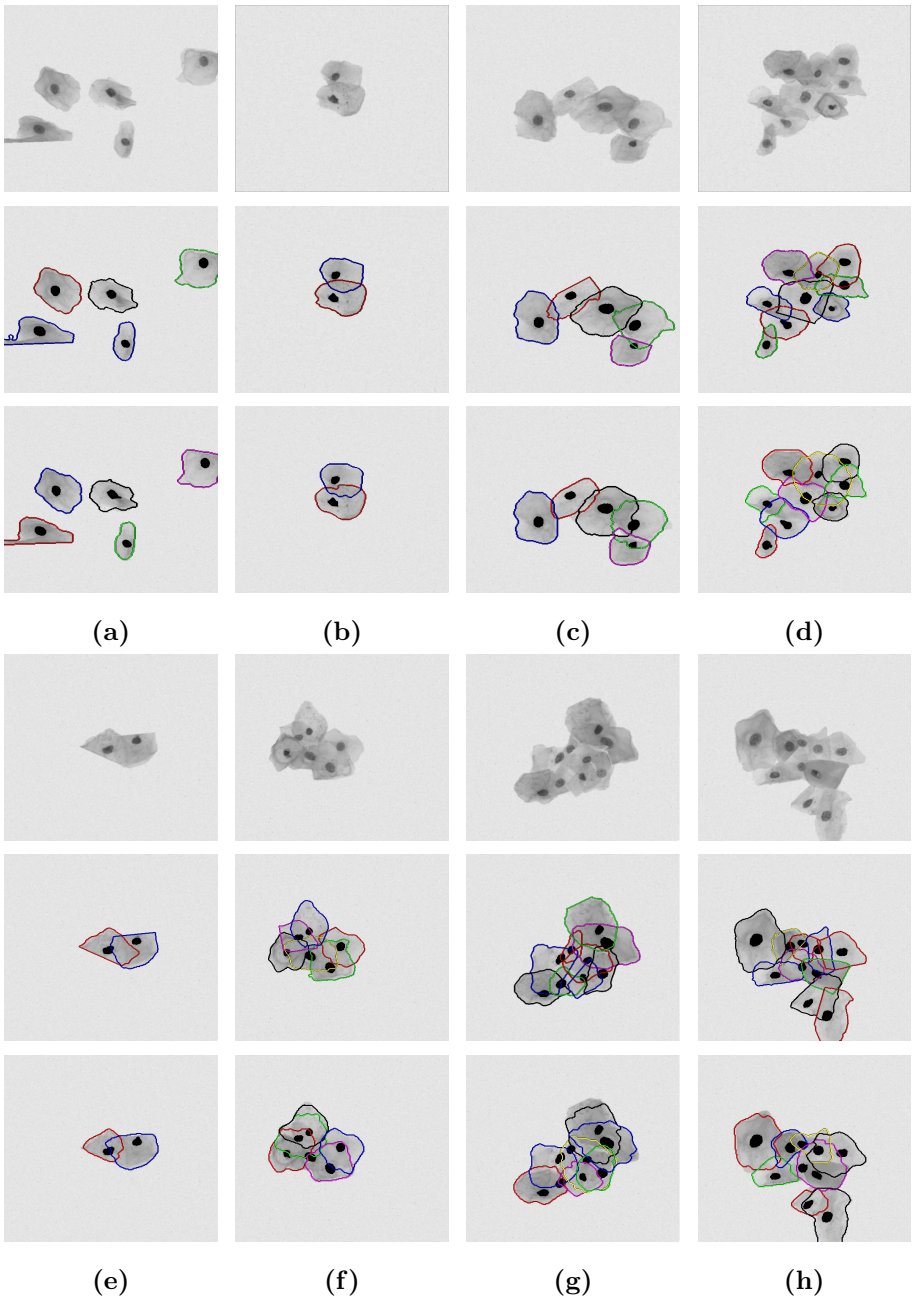

Figure 9: Examples of the nuclei and cytoplasm segmentation. The first row in each group shows the original cervical image, the second row shows the ground truth of the cells, and the third row shows the segmentation results of our approach for different cell structures. The nuclei are highlighted in black color, and the contours are outlined by red, green, blue, black, yellow, and purple color.

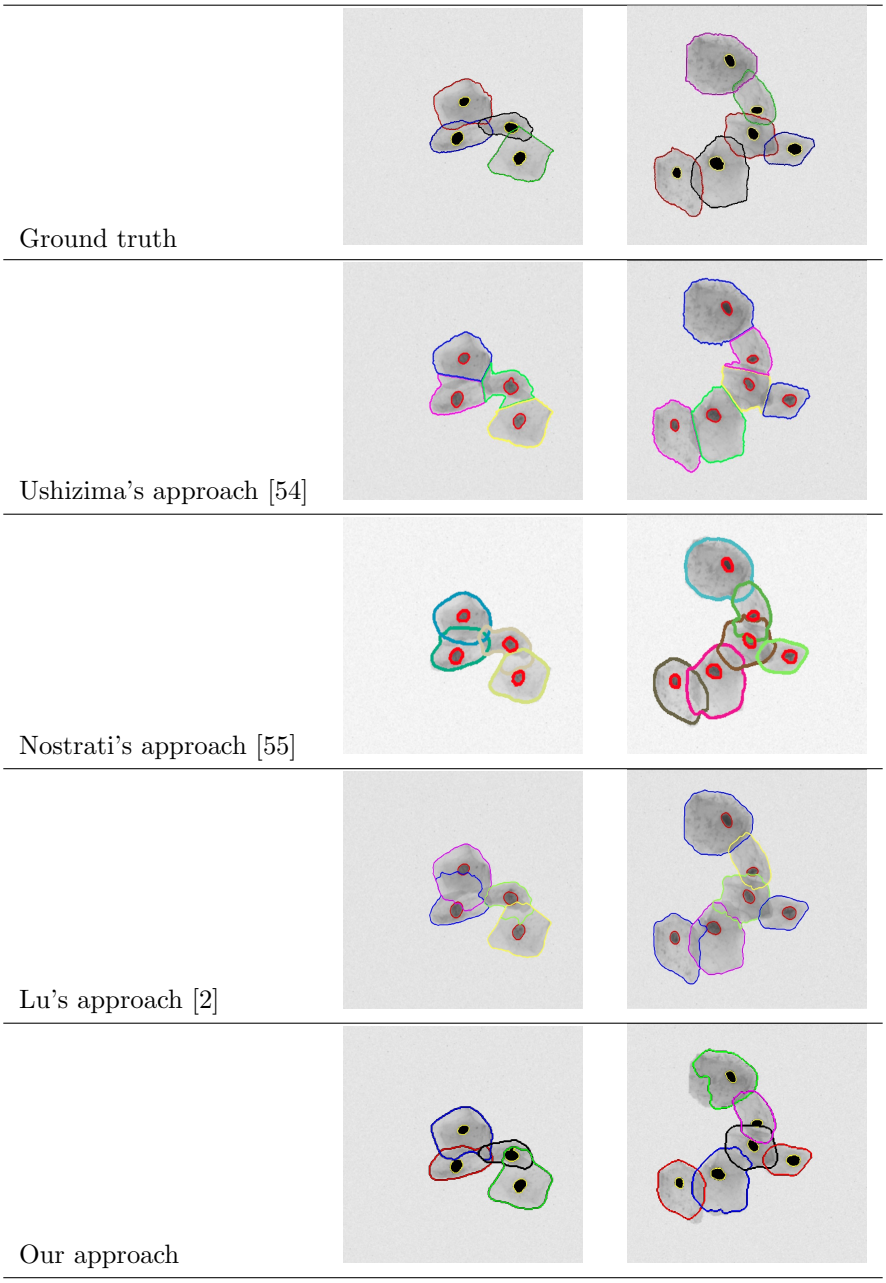

Figure 10: Qualitative evaluation of the proposed approach and the ISBI challenge methods [56].

mation process, whereas the refinement and filtering time is the execution time for DRLSE-based refinement step and the false candidates filtering step.

The proposed approach took 18 seconds on average to classify the Pap smear image to its cellular components, and approximately 10 seconds to segment each cell in the image. The execution time of the second stage varied depending on the cell structure. For instance, the second stage of our approach needs less than one second to segment each isolated cell, as there was no need to establish the edge maps or use the shape deformation process. The alternative initialization process, in cases where the edge maps failed to generate the initial shapes, also influenced the processing time. Our method was approximately twice as fast as Lu et al.'s technique, which took, on average, 56 seconds per cell. This improvement in the time complexity is mainly attributed to two points: 1) using the superpixels instead of the image pixels in the classification stage; 2) the robust edge-based initialization of the cytoplasm shape, which reduces the number of iterations needed in the sparse deformation and refinement stages. Moreover, the simplicity of the isolated cytoplasm segmentation procedure, and ignoring unnecessary steps, help in improving the time complexity of our approach.

Table 7: Execution time of the proposed approach

The proposed approach steps	Time in sec./cell
Nuclei segmentation stage	18.25 ± 0.42
Cell segmentation stage	
Edge establishment	3.51 ± 2.56
Sparse shape deformation	2.47 ± 1.75
Refinement and filtering	3.20 ± 0.19

5.5. Evaluation of the Deformation Process

The performance improvement of our guided shape deformation process over the conventional deformation process is shown in Table 8. We compared the segmentation results of our approach with the results of the deformable DRLSE model with a conventional initialization (e.g., the circular mask established by

Eq. (5) above); let be called conventional DRLSE. As explained in Section 5.2, the high FNo led to higher TPp and DC, since only the well-segmented cells were used in evaluation. This explains the acceptable DC rate of the conventional DRLSE. The high TPp resulted from the larger cell regions that were detected. The cytoplasm initialization and deformation process we employed further improved the results of the deformable model using the same initial circular mask. We obtained around half of the FNo obtained using the conventional mask and improved the DC by 5%. Our shape initialization and approximation process reduced the execution time by using 50 iterations to refine the cytoplasm contour. Whereas, two hundred iterations were needed when using the conventional DRLSE (i.e., increasing the number of iterations could not enhance the results).

It is generally accepted that the effectiveness of deformable models is affected mainly by the contour initialization process. Pap smears, usually contain cytoplasmic regions that show lower intensities than the surrounding areas. When deformable models reach such regions in search of the cell boundary, they slow down or stop. There can also be too many nuclei in an ROI that force the deformable model to stop. Moreover, deformable models cannot distinguish between the edges of the cell in focus and the edges of the neighbouring cells. In the end, the false positives and irregularly-shaped cytoplasm are increased. Our deformable approach succeeded in providing a solution for outlining complex objects where there are marked overlaps and variations in shape.

Table 8: Evaluation of the performance improvement obtained by the SC-based deformation process.

Measures	Conventional approach	Our approach
DC	0.84 ± 0.08	0.89 ± 0.07
TPp	0.94 ± 0.03	0.91 ± 0.09
FPp	0.01 ± 0.01	0.00 ± 0.01
FNo	0.48 ± 0.32	0.25 ± 0.25

6. Conclusions

The segmentation of cervical cell smears is an ill-posed problem because of the varied shape and often significant overlap. In this paper we have presented a 2-stage segmentation approach that addresses this challenging problem using distinctive superpixel-based shape and appearance features, and a guided sparse shape deformation process using representative feature points. Applying superpixeling with high regularity to exploit the shape property of the superpixels in classification, along with discriminative texture and boundary features, has great influence in obtaining accurate nuclear segmentation, and precise cytoplasm/background boundaries. Moreover, the shape initialization process, and using the feature points to approximate the cell shape, provide a successful solution to tackle the difficulties of using sparse deformation with Pap smear images, due to the large variation in the cell shapes and their high degree of overlapping. Our shape initialization procedure is adaptable and able to work with the different cell types (i.e., simple process based on classification results for isolated cells, two mask candidates for more complex cell structure, and carefully-computed alternative cell mask for the fuzzy cells without extractable edges). The qualitative and quantitative results demonstrated the practicality and reliability of our approach in segmenting not only the isolated and touching cells, but also cells from large clusters with high degree of overlapping. Our approach offers improvements over existing techniques in accuracy and speed of computation. In the future work, we intend to apply our approach to stacks of multi-focal images [57].

References

[1] World cancer report 2014, World Health Organization (2014) Chapter 5.12.

[2] Z. Lu, G. Carneiro, A. P. Bradley, An improved joint optimization of multiple level set functions for the segmentation of overlapping cervical cells, Image Processing, IEEE Transactions on 24 (4) (2015) 1261–1272.

[3] H.-S. Wu, J. Gil, J. Barba, Optimal segmentation of cell images, in: Vision, Image and Signal Processing, IEE Proceedings-, Vol. 145, IET, 1998, pp. 50–56.

[4] N. Béliz-Osorio, J. Crespo, M. García-Rojo, A. Muñoz, J. Azpiazu, Cytology imaging segmentation using the locally constrained watershed transform, in: Mathematical Morphology and Its Applications to Image and Signal Processing, Springer, 2011, pp. 429–438.

[5] K. Li, Z. Lu, W. Liu, J. Yin, Cytoplasm and nucleus segmentation in cervical smear images using radiating GVF snake, Pattern Recognition 45 (4) (2012) 1255–1264.

[6] J. Fan, R. Wang, S. Li, C. Zhang, Automated cervical cell image segmentation using level set based active contour model, in: Control Automation Robotics & Vision (ICARCV), 2012 12th International Conference on, IEEE, 2012, pp. 877–882.

[7] S.-F. Yang-Mao, Y.-K. Chan, Y.-P. Chu, Edge enhancement nucleus and cytoplast contour detector of cervical smear images, Systems, Man, and Cybernetics, Part B: Cybernetics, IEEE Transactions on 38 (2) (2008) 353–366.

[8] T. Chankong, N. Theera-Umpon, S. Auephanwiriyakul, Automatic cervical cell segmentation and classification in pap smears, Computer Methods and Programs in Biomedicine 113 (2) (2014) 539–556.

[9] L. Zhang, H. Kong, C. T. Chin, S. Liu, Z. Chen, T. Wang, S. Chen, Segmentation of cytoplasm and nuclei of abnormal cells in cervical cytology using global and local graph cuts, Computerized Medical Imaging and Graphics 38 (5) (2014) 369–380.

[10] L. Zhang, H. Kong, C. T. Chin, T. Wang, S. Chen, Cytoplasm segmentation on cervical cell images using graph cut-based approach, Bio-Medical Materials and Engineering 24 (1) (2014) 1125–1131.

[11] M. E. Plissiti, C. Nikou, A. Charchanti, Automated detection of cell nuclei in pap smear images using morphological reconstruction and clustering, Information Technology in Biomedicine, IEEE Transactions on 15 (2) (2011) 233–241.

[12] M. Hu, X. Ping, Y. Ding, Automated cell nucleus segmentation using improved snake, in: Image Processing, 2004. ICIP'04. 2004 International Conference on, Vol. 4, IEEE, 2004, pp. 2737–2740.

[13] C. Bergmeir, M. García Silvente, J. M. Benítez, Segmentation of cervical cell nuclei in high-resolution microscopic images: A new algorithm and a web-based software framework, Computer Methods and Programs in Biomedicine 107 (3) (2012) 497–512.

[14] M. E. Plissiti, C. Nikou, Overlapping cell nuclei segmentation using a spatially adaptive active physical model, Image Processing, IEEE Transactions on 21 (11) (2012) 4568–4580.

[15] C. Jung, C. Kim, Segmenting clustered nuclei using H-minima transform-based marker extraction and contour parameterization, Biomedical Engineering, IEEE Transactions on 57 (10) (2010) 2600–2604.

[16] M. E. Plissiti, C. Nikou, A. Charchanti, Combining shape, texture and intensity features for cell nuclei extraction in Pap smear images, Pattern Recognition Letters 32 (6) (2011) 838–853.

[17] C. Jung, C. Kim, S. W. Chae, S. Oh, Unsupervised segmentation of overlapped nuclei using bayesian classification, Biomedical Engineering, IEEE Transactions on 57 (12) (2010) 2825–2832.

[18] A. Gentav, S. Aksoy, S. nder, Unsupervised segmentation and classification of cervical cell images, Pattern Recognition 45 (12) (2012) 4151–4168.

[19] A. Kale, S. Aksoy, Segmentation of cervical cell images, in: Pattern Recognition (ICPR), 2010 20th International Conference on, IEEE, 2010, pp. 2399–2402.

[20] A. Tareef, Y. Song, W. Cai, D. Feng, M. Chen, Automated three-stage nucleus and cytoplasm segmentation of overlapping cells, in: Control Automation Robotics & Vision (ICARCV), 2014 13th International Conference on, IEEE, 2014, pp. 865–870.

[21] Z. Lu, G. Carneiro, A. P. Bradley, Automated nucleus and cytoplasm segmentation of overlapping cervical cells, in: Medical Image Computing and Computer-Assisted Intervention–MICCAI 2013, Springer, 2013, pp. 452–460.

[22] M. Nosrati, G. Hamarneh, Segmentation of overlapping cervical cells: A variational method with star-shape prior, in: IEEE International Symposium on Biomedical Imaging (ISBI), IEEE, 2015.

[23] T. F. Cootes, C. J. Taylor, D. H. Cooper, J. Graham, Active shape models-their training and application, Computer vision and image understanding 61 (1) (1995) 38–59.

[24] H. Cai, X. Xu, J. Lu, J. Lichtman, S. Yung, S. T. Wong, Shape-constrained repulsive snake method to segment and track neurons in 3d microscopy images, in: 3rd IEEE International Symposium on Biomedical Imaging: Nano to Macro, 2006., IEEE, 2006, pp. 538–541.

[25] F. Xing, Y. Xie, L. Yang, An automatic learning-based framework for robust nucleus segmentation, IEEE transactions on medical imaging 35 (2) (2016) 550–566.

[26] S. Ali, A. Madabhushi, An integrated region-, boundary-, shape-based active contour for multiple object overlap resolution in histological imagery, IEEE transactions on medical imaging 31 (7) (2012) 1448–1460.

[27] S. Ali, R. Veltri, J. I. Epstein, C. Christudass, A. Madabhushi, Selective invocation of shape priors for deformable segmentation and morphologic classification of prostate cancer tissue microarrays, Computerized Medical Imaging and Graphics 41 (2015) 3–13.

[28] F. Xing, L. Yang, Robust selection-based sparse shape model for lung cancer image segmentation, in: Medical Image Computing and Computer-Assisted Intervention–MICCAI 2013, Springer, 2013, pp. 404–412.

[29] X. Qi, F. Xing, D. J. Foran, L. Yang, Robust segmentation of overlapping cells in histopathology specimens using parallel seed detection and repulsive set, Biomedical Engineering, IEEE Transactions on 59 (3) (2012) 754–765.

[30] W. Srisang, K. Jaroensutasinee, M. Jaroensutasinee, Segmentation of overlapping chromosome images using computational geometry, Walailak Journal of Science and Technology (WJST) 3 (2) (2011) 181–194.

[31] P. Quelhas, M. Marcuzzo, A. M. Mendona, A. Campilho, Cell nuclei and cytoplasm joint segmentation using the sliding band filter, Medical Imaging, IEEE Transactions on 29 (8) (2010) 1463–1473.

[32] R. Achanta, A. Shaji, K. Smith, A. Lucchi, P. Fua, S. Susstrunk, SLIC superpixels compared to state-of-the-art superpixel methods, Pattern Analysis and Machine Intelligence, IEEE Transactions on 34 (11) (2012) 2274–2282.

[33] K. Zuiderveld, Contrast limited adaptive histogram equalization, in: Graphics gems IV, Academic Press Professional, Inc., 1994, pp. 474–485.

[34] M. Yang, K. Kpalma, J. Ronsin, A survey of shape feature extraction techniques, Pattern recognition (2008) 43–90.

[35] W. Gonzalez, R. E. Woods, Eddins, digital image processing using matlab, Third New Jersey: Prentice Hall.

[36] J. Canny, A computational approach to edge detection, Pattern Analysis and Machine Intelligence, IEEE Transactions on (6) (1986) 679–698.

[37] R. M. Haralock, L. G. Shapiro, Computer and robot vision, Addison-Wesley Longman Publishing Co., Inc., 1991.

[38] C.-C. Chang, C.-J. Lin, Libsvm: a library for support vector machines, ACM Transactions on Intelligent Systems and Technology (TIST) 2 (3) (2011) 27.

[39] Y. Song, W. Cai, D. D. Feng, Microscopic image segmentation with two-level enhancement of feature discriminability., in: International Conference on Digital Image Computing: Techniques and Applications (DICTA), 2012, pp. 1–6.

[40] Y. Song, W. Cai, D. D. Feng, M. Chen, Cell nuclei segmentation in fluorescence microscopy images using inter-and intra-region discriminative information, in: Engineering in Medicine and Biology Society (EMBC), 35th Annual International Conference of the IEEE, IEEE, 2013, pp. 6087–6090.

[41] Y. Song, W. Cai, H. Huang, Y. Wang, D. D. Feng, Object localization in medical images based on graphical model with contrast and interest-region terms, in: Computer Vision and Pattern Recognition Workshops (CVPRW), IEEE Computer Society Conference on, IEEE, pp. 1–7.

[42] Y. Song, W. Cai, H. Huang, Y. Wang, D. D. Feng, M. Chen, Region-based progressive localization of cell nuclei in microscopic images with data adaptive modeling, BMC Bioinformatics 14 (1) (2013) 173.

[43] S. M. Smith, Bet: brain extraction tool, FMRIB TR00SMS2b, Oxford Centre for Functional Magnetic Resonance Imaging of the Brain), Department of Clinical Neurology, Oxford University, John Radcliffe Hospital, Headington, UK.

[44] C. Goodall, Procrustes methods in the statistical analysis of shape, Journal of the Royal Statistical Society. Series B (Methodological) (1991) 285–339.

[45] S. Zhang, Y. Zhan, M. Dewan, J. Huang, D. N. Metaxas, X. S. Zhou, Deformable segmentation via sparse shape representation, in: Medical Image Computing and Computer-Assisted Intervention–MICCAI 2011, Springer, 2011, pp. 451–458.

[46] C. Florin, N. Paragios, G. Funka-Lea, J. Williams, Liver segmentation using sparse 3D prior models with optimal data support, in: Information Processing in Medical Imaging, Springer, 2007, pp. 38–49.

[47] Y. Gao, S. Liao, D. Shen, Prostate segmentation by sparse representation based classification, Medical Physics 39 (10) (2012) 6372–6387.

[48] G. Gill, M. Toews, R. R. Beichel, Robust initialization of active shape models for lung segmentation in CT scans: A feature-based atlas approach, International Journal of Biomedical Imaging 2014.

[49] D. L. Donoho, Y. Tsaig, I. Drori, J.-L. Starck, Sparse solution of underdetermined systems of linear equations by stagewise orthogonal matching pursuit, Information Theory, IEEE Transactions on 58 (2) (2012) 1094–1121.

[50] S. Umeyama, Least-squares estimation of transformation parameters between two point patterns, IEEE Transactions on Pattern Analysis and Machine Intelligence 13 (4) (1991) 376–380.

[51] S. W. Smith, "Moving average filters", in The Scientist and Engineer's Guide to Digital Signal Processing, California Technical Pub. San Diego, 1997, Ch. 15, pp. 277–284.

[52] C. Li, C. Xu, C. Gui, M. D. Fox, Distance regularized level set evolution and its application to image segmentation, Image Processing, IEEE Transactions on 19 (12) (2010) 3243–3254.

[53] Overlapping Cervical Cytology Image Segmentation Challenge-ISBI 2014, `http://cs.adelaide.edu.au/~carneiro/isbi14_challenge/`.

[54] D. Ushizima, A. Bianch, C. Carneiro, Segmentation of subcellular compartiments combining superpixel representation with voronoi diagrams, in: ISBI Overlapping Cervical Cytology Image Segmentation Challenge, IEEE, 2014, pp. 1–2.

[55] M. Nosrati, G. Hamarneh, A variational approach for overlapping cell segmentation, in: ISBI Overlapping Cervical Cytology Image Segmentation Challenge, IEEE, 2014, pp. 1–2.

[56] Z. Lu, G. Carneiro, A. Bradley, D. Ushizima, M. Nosrati, A. Bianchi, C. Carneiro, G. Hamarneh, Evaluation of three algorithms for the segmentation of overlapping cervical cells., IEEE Journal of Biomedical and Health Informatics, 2016.

[57] The Second Overlapping Cervical Cytology Image Segmentation Challenge-ISBI 2015, http://cs.adelaide.edu.au/~zhi/isbi15_challenge/.